Principles of operation of a passively mode-locked fiber ring laser and 3D mapping of ultra-short pulses

H.E. Ibarra-Villalón[a,b], O. Pottiez[b], Y.E. Bracamontes-Rodriguez[b], J.P. Lauterio-Cruz[c] and A. Gomez-Vieyra[d]
[a]*Posgrado en Física. Universidad Autónoma Metropolitana-Unidad Iztapalapa,*
San Rafael Atlixco No. 186, Col. Vicentina, Iztapalapa, 09340, México.
e-mail: alm.hugoibarra@gmail.com
[b]*Centro de Investigaciones en Óptica A. C.*
Lomas del Bosque 115, Col. Lomas del Campestre, León Gto. 37150, México.
[c]*Departamento de Electrónica, DICIS-Universidad de Guanajuato,*
Carr. Salamanca-Valle de Santiago km 3.5+1.8, Comunidad de Palo Blanco, Salamanca, Gto. 36885, México.
[d]*Departamento de Ciencias Básicas e Ingeniería, Universidad Autónoma Metropolitana, Unidad Azcapotzalco*
Av. San Pablo No. 180. Col. Reynosa Tamaulipas, 02200, Azcapotzalco, CDMX. México.

Received 4 January 2018; accepted 14 February 2018

In this article, we study the operation and basic elements in a passively mode-locked fiber ring laser (PML-FRL), emphasizing the saturable absorber (SA) effect seen as a nonlinear filter in transmission, which is produced by the non-linear polarization rotation (NPR) and a linear polarizer. Besides, we employ a technique of 3D mapping measurements for characterizing ultra-short pulse dynamics.

Keywords: Mode locked fiber laser; saturable absorber; nonlinear fiber optics; pulse dynamics.

PACS: 42.55.Wd; 42.65.Re.

1. Introduction

A mode-locked fiber laser (ML-FL) is a device that is able to produce short and ultra-short optical pulses (ns and fs-ps). This kind of pulse finds applications in pressure sensors [1,2], gas sensors [3], micromachining of materials [4], and supercontinuum generation [5, 6], among others. However, there are many implicit effects in the formation and generation of ultra-short pulses, which possibly limit their use for some specific applications. For this reason, the study of the generation and dynamics of ultra-short pulses in a ML-FL remains a hot research topic.

To achieve pulsed operation, we can use for instance the mode locking technique. It divides into two categories: the first one is passive mode locking [7–9], which relies on a mechanism of modulation of cavity losses that operates by itself, without external intervention; the second one is active mode locking [10, 11], which uses an externally driven acousto-optic or electro-optic element that produces a controlled modulation of losses in time.

In a passively mode-locked fiber laser (PML-FL), the gain medium and saturable absorber (SA) initiate the pulsing operation. The SA is an optical device that functions as a nonlinear filter which absorbs low-power radiation and transmits high-power component of a signal. The SA can be classified in function of their saturation time; when the time response of the SA is shorter than the pulse duration, it is known as fast saturable absorber (FSA) [12–14]; when its time response is longer, it is known as slow saturable absorber (SSA) [15,16].

Commonly, for introducing a power-selective loss, PML-FLs include a physical SA, like the semiconductor saturable absorber mirror (SESAM) [16–18], the most commonly used, although the SESAM has the inconvenient that it usually generates pulses with low energy. Besides, quantum dots embedded in a semiconductor material are used as SA in ML-FLs [19,20] generating low saturation fluence. On the other hand, physical SAs have also been implemented from carbon nanotubes [21,22], with which high pulse repetition rates can be generated in a compact cavity. Besides, graphene SAs have been implemented in femtosecond pulse generation [23,24].

Other PML-FLs have a figure-eight or ring configuration; for these architectures, usually an artificial SA is used, which relies on non-linear effects generated in optical fiber, so indirectly the absorbed energy through to a laser component (commonly a polarizer or an isolator) is reduced by the changes that produces the non-linear effect. The Non-linear Optical Loop Mirror (NOLM) [6,25,26], the Non-linear Amplifying Loop Mirror (NALM) [28,35] or the Non-linear Polarization Rotation (NPR) [9, 29] effect are examples of artificial SA implemented in PML-FLs. Commonly, the NPR effect is the SA meachanism used in a passively mode-locked fiber ring laser (PML-FRL); the latter is studied in this paper.

In recent years, the dynamics of pulses generated by ML-FL have been studied with experimental analysis and theoretical models. Different behaviors and interactions of pulses have been investigated, which encompass different types of pulses: noise-like pulses (NLPs) [6, 25, 26, 28], dissipative solitons [30, 31], spiny solitons [32], among others. A recently developed tool, which is useful in ML-FL researches, is a 3D mapping technique of the pulse temporal profile, which helps analyzing pulse dynamics [31, 33–36].

In this paper, we implement a theoretical analysis of the 3D mapping of a pulse conglomerate and of a single pulse (shorter-wavelength component and longer-wavelength com-

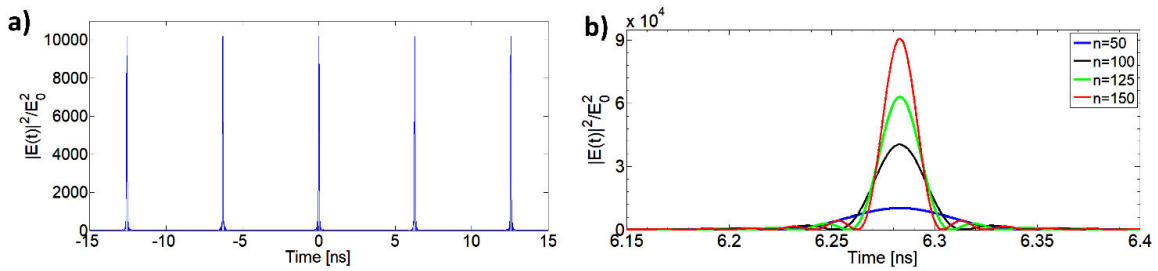

FIGURE 1. a) Total electric field intensity in presence of the mode-locking mechanism over 4 consecutive periods. b) Curve of the dimensionless intensity at different number of modes $(2n+1)$.

ponent, respectively) in anomalous and normal dispersion regimes of a ML-FL. This study helps us to interpret the 3D mapping measurements in terms of pulse dynamics. Besides, an example of experimental 3D mapping measurement is presented in the case of a regime where a NLP coexists with bunches of solitons generated by a PML-FRL.

2. Theoretical model of the mode-locking by the superposition principle of the electric field

One of the most common models to explain the generation of short pulses by mode-locking will be presented [37]. Mode locking means that all modes propagating in the optical fiber resonator are locked in phase; in a model of $2n+1$ modes with the same amplitude E_0, the mode-locking is imposed by the condition of constant phase between two consecutive modes, written as

$$\triangle\phi = \phi_l - \phi_{l-1} = c_1 \tag{1}$$

where: $l = -n, -n+1, \ldots, 0, \ldots, n-1, n$, and c_1 is a constant. The total electric field associated with the $2n+1$ modes is

$$E(t) = \sum_{l=-n}^{l=n} E_0 e^{i((\omega_0 + l\triangle\omega)t + l\triangle\phi)} \tag{2}$$

where the difference in frequency between 2 consecutive modes is constant $\triangle\omega = c_2$. Eq. (2) gives information that the total electric field is centered at a frequency ω_0; so the mathematical structure can be written as

$$E(t) = A(t)e^{i\omega_0 t} \tag{3}$$

where:

$$A(t) = \sum_{l=-n}^{l=n} E_0 e^{il(\triangle\omega t + \triangle\phi)} \tag{4}$$

The amplitude A(t) is simplified by the geometrical progression given by

$$\sum_{k=m}^{k=n} af^k = a\frac{f^m - f^{n+1}}{1-f} \tag{5}$$

where in this case $f = e^{i(\triangle\omega t + \triangle\phi)}$. This simplification transforms the mathematical expression of the total electric field from Eq. (2) to Eq. (6); the latter will help us to understand the mode-locking process.

The total electric field at the output laser is represented as

$$E(t) = E_0 \frac{\sin(\frac{2n+1}{2}(\triangle\omega t + \triangle\phi))}{\sin(\frac{\triangle\omega t + \triangle\phi}{2})} e^{i\omega_0 t}, \tag{6}$$

and its mathematical structure is the result of imposing the condition of mode-locking (all modes are in phase or locked); so it is expected that the field intensity $I = |E(t)|^2$ is a periodic train of pulses, as shown in Fig. 1a, which plots the dimensionless intensity $(|E(t)|^2/E_0^2)$ versus time, considering the parameters: $\triangle\phi = 2\pi, \triangle\omega = 10^9 rad/s$ and the total number of modes $2n+1 = 101$. It is important to remark that the Eq. (6) presents a discontinuous at $t = 0$, but it is clearly, which at $t \ll 1$, the consideration of $sin(\beta) \approx \beta$ where $\beta \ll 1$ is used, so the dimensionless intensity is approximated to $|E(t)|^2/E_0^2 \approx (2n+1)^2 = 10201$. On the other hand, the dimensionless intensity gives us information that to a larger number of modes $(2n+1)$ the pulse reaches a higher intensity, as well as a narrower temporal width, as shown in Fig. 1b.

3. The operation principles in a PML-FRL

The operation of a fiber ring laser (FRL) with passive mode locking is possible thanks to the use of specific optical elements and non-linear effects; these will be explained in this Section.

All lasers consist of three main parts: a gain medium, an external pumping, and a resonant cavity; the latter makes possible the laser beam emission; in the present case, the cavity is a fiber ring. The resonance mechanism in the FRL starts with an initial signal, generated in the cavity, which is amplified at each round-trip until its energy remains stable. The basic elements in a PML-FRL are shown in Fig. 2, the cavity consists of a SA, a gain medium, the chromatic dispersion effect (introduced by the fiber), a polarization controller, an optical isolator (which allows the beam propagation to be unidirectional), output coupler and the nonlinear optical effects (also produced by the fiber).

The gain medium, in turn, consists of an optical fiber doped with a rare-earth element (the most common doped

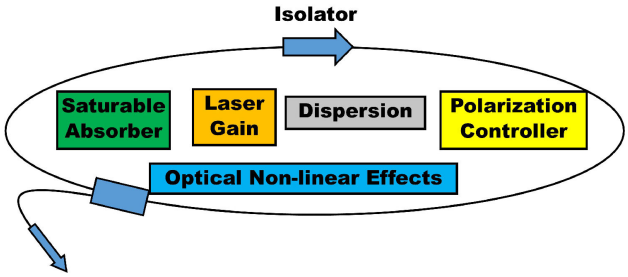

FIGURE 2. Scheme of the basics elements in a PML-FRL.

fiber used in communications is the erbium-doped fiber (EDF) [38]) fed by an optical pump, which in this case can be a laser diode coupled with the doped fiber; the laser diode emits at a wavelength at which the ions of the doped fiber present strong absortion.

The chromatic dispersion is an effect that occurs in a transparent medium, in this case, a silica optical fiber. This effect causes the phase velocity and the group velocity of the light propagating in fiber to be dependent on the optical frequency [39]. The origin of chromatic dispersion is the variation of the refractive index as a function of the wavelength of light. The most usual and economic form to introduce chromatic dispersion in the ring cavity is by inserting several meters of standard single mode fiber (SMF). This type of fiber will introduce anomalous chromatic dispersion; this kind of dispersion causes the refraction index to increase if the wavelength increases; in other words, the longer-wavelength components travel slower with respect to the shorter-wavelength components. On the other hand, it is possible to use dispersion compensating fiber, which introduces normal dispersion in the PML-FRL; this means that the longer-wavelength components travel in this case faster than the shorter-wavelengths.

In the context of the nonlinear effects, when the pulse propagates in the optical fiber with high intensity, a phenomenon called the Kerr effect takes place: it produces a dependence of the refractive index as function of the intensity I [40] as follows:

$$n = n_0 + n_2 I \tag{7}$$

where n_0 is the refractive index at low-power and n_2 is the nonlinear coefficient.

One of the fundamental elements in the ML-FL is the SA, introduced in the first Section. Its action is that of a nonlinear filter that absorbs the low-intensity components of a signal, and transmits the high-intensity components, which are able to saturate the device; for this reason, the SA favors the generation of short or ultrashort pulses by the laser.

The SA in the PML-FRL is produced through the effect of the non-linear polarization rotation (NPR) and the use of a linear polarizer inserted in the cavity. The SA principle is explained by the scheme in Fig. 3, first an elliptical polarization state is imposed; this condition can be achieved with the polarization controller (array of polarizers and wave retarder plates). In the first case, at low power (Fig. 3a), the elliptical polarization state does not undergo NPR, this means that the initial polarization state does not change during propagation; besides, if its major axis is orthogonal to the polarizer axis, then the transmission is nearly zero. In the second case, at high powers (Fig. 3b), the components of the elliptical polarization state propagating in the fiber induce a nonlinear birefringence; the latter will cause the elliptical polarization state to rotate as it propagates: this is the essence of the NPR effect [41]. One way to visualize NPR is using the representation of the Stokes vector on the Poincare sphere; NPR corresponds to a rotation around axis S_3 [42], as shown in Fig. 4.

So, recapitulating the scheme of Fig. 3b, the main idea of the SA (nonlinear filter) is that the elliptical polarization state crosses the linear polarizer, hence the transmission is maximum when the major axis of the ellipse is aligned with the orientation of the polarizer (which occurs at high power, due

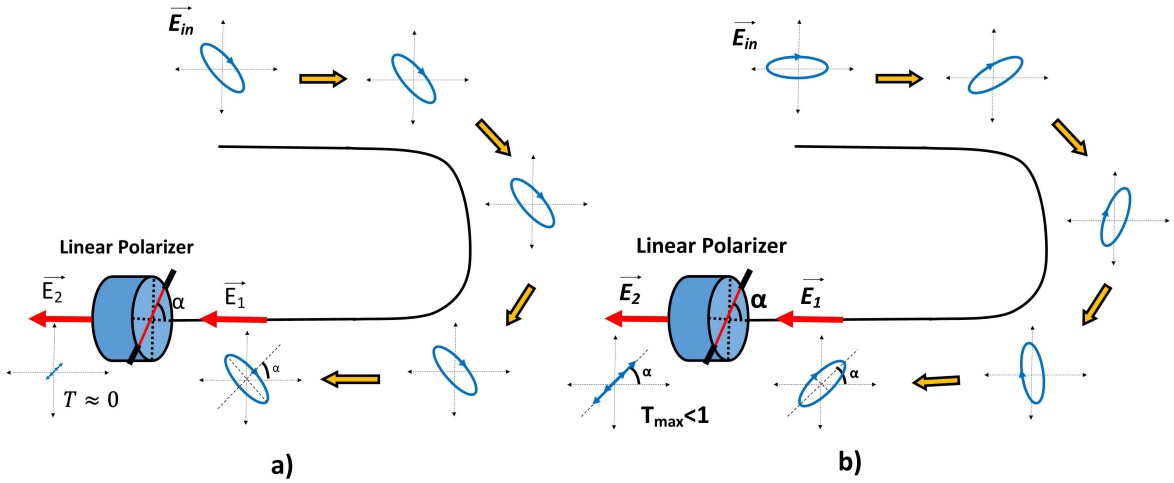

FIGURE 3. Scheme of the SA mechanism by the NPR in elliptical polarization state and linear polarizer: a) low-powers (without the NPR, there is no SA effect). b) high-powers (with the NPR there is a SA effect).

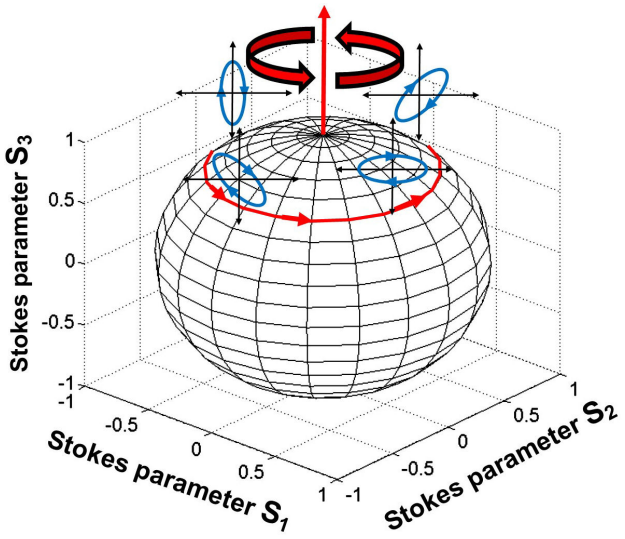

FIGURE 4. Representation of the NPR in the Poincare sphere.

to NPR), and is minimal if the major axis is perpendicular to the polarizer (at low power, when no NPR takes pace). Hence, the transmission through the linear polarizer depends on the power of the incident beam.

The saturable absorption effect is analyzed by calculating the transmission through the linear polarizer: $T = |E_2|^2/|E_1|^2$. For this purpose, it is necessary to study the evolution of the polarization state components in the formalism of the Jones vector in a circular polarization base $\{C_+, C_-\}$. The analysis starts with the definition of the Jones vector of the initial polarization state with an initial power P

$$E_{in} = \sqrt{P}\begin{pmatrix} ue^{i\psi} \\ ve^{-i\psi} \end{pmatrix} \tag{8}$$

where ψ is the orientation of the polarization state with respect to the horizontal axis and u and v are real parameters fulfilling the condition $u^2 + v^2 = 1$, for an elliptical polarization state $u \neq v$.

The propagation of the initial polarization state (Eq. (8)) is considered in an ideal case for an isotropic fiber of length L. The contribution of the nonlinear phase is $e^{i\phi} = e^{i\gamma_N PL}$ and the NPR is e^{ir} with $r = -(1/3)\gamma_N P A_c L$ (see Appendix A). In the scheme of Fig. 3b, the polarization state previous to the linear polarizer is given by the following expression

$$\begin{aligned} E_1 &= \sqrt{P}\begin{pmatrix} e^{i(\phi+r)} & 0 \\ 0 & e^{i(\phi-r)} \end{pmatrix}\begin{pmatrix} ue^{i\psi} \\ ve^{-i\psi} \end{pmatrix} \\ &= \sqrt{P}\begin{pmatrix} ue^{i(\phi+r+\psi)} \\ ve^{i(\phi-r-\psi)} \end{pmatrix} \end{aligned} \tag{9}$$

The polarization state E_1 passes through the linear polarizer; the latter is oriented with an angle α with respect to the horizontal axis. Hence, at the output of the polarizer, the following polarization state E_2 is obtained

$$\begin{aligned} E_2 &= [P_{L_\alpha}]_C E_1 \\ &= \frac{1}{2}\sqrt{P}e^{i\phi}\begin{pmatrix} ue^{i(\psi+r)} + ve^{-i(\psi+r-2\alpha)} \\ ue^{i(\psi+r-2\alpha)} + ve^{-i(\psi+r)} \end{pmatrix} \end{aligned} \tag{10}$$

with the transformation matrix of the linear polarizer, we have

$$[P_{L_\alpha}]_C = \frac{1}{2}\begin{pmatrix} 1 & e^{2i\alpha} \\ e^{-2i\alpha} & 1 \end{pmatrix} \tag{11}$$

Finally, the mathematical expression of the linear polarizer transmission is given by

$$T = \frac{|E_2|^2}{|E_1|^2} = \frac{1}{2} + uv\cos(2(\psi + r - \alpha)) \tag{12}$$

In Eq. (12), a dependence of the NPR appears associated with the term $r = -(1/3)\gamma_{NL} P A_c L$. This expression of the transmission explains the reason to impose the condition of the elliptical polarization state, because if the initial polarization state is circular (right circular with $u = 1$, $v = 0$ and $A_c = 1$ or left circular $u = 0$, $v = 1$ and $A_c = -1$), the transmission is constant versus power ($T = 1/2$). On the other hand, if the initial polarization state is linear and oriented with an angle ψ with respect to the horizontal axis, the transmission of the linear polarizer depends on the orientation of the polarizer and the orientation of the linear polarization state

$$T = \frac{1}{2} + \frac{1}{2}\cos(2(\psi - \alpha)) \tag{13}$$

however, in this case, no NPR takes place ($r = 0$), so that again, the transmission remains constant versus power.

The expression for the transmission of the linear polarizer helps understanding the effect of SA when representing the transmission as a function of the power of the elliptical polarization state ($u \neq v$ and $A_c \neq 0$). If the minor axis of incident polarization is nearly orthogonal to the polarizer axis, the transmission is that of a high pass filter (high powers are transmitted, and low powers are absorbed); for example, Fig. 5a shows the curve of transmission as function of power for the case of a horizontal elliptical polarization state, given by

$$E_{in} = \sqrt{P}\begin{pmatrix} \frac{2}{\sqrt{5}} \\ \frac{1}{\sqrt{5}} \end{pmatrix} \tag{14}$$

which propagates through an isotropic fiber of length $L = 100\ m$ with a nonlinear coefficient $\gamma_N = 1.5\ \text{km}^{-1}\text{W}^{-1}$ and the linear polarizer oriented along of the vertical axis ($\alpha = 90°$). In this case the expression of the transmission is given by

$$T = \frac{1}{2} - \frac{2}{5}\cos(\frac{2}{3}\gamma_N P A_c L) \tag{15}$$

with the maximum transmission reached at the critical power $P_\pi = (3\pi)/(2\gamma_N A_c L) = 52.35$ W.

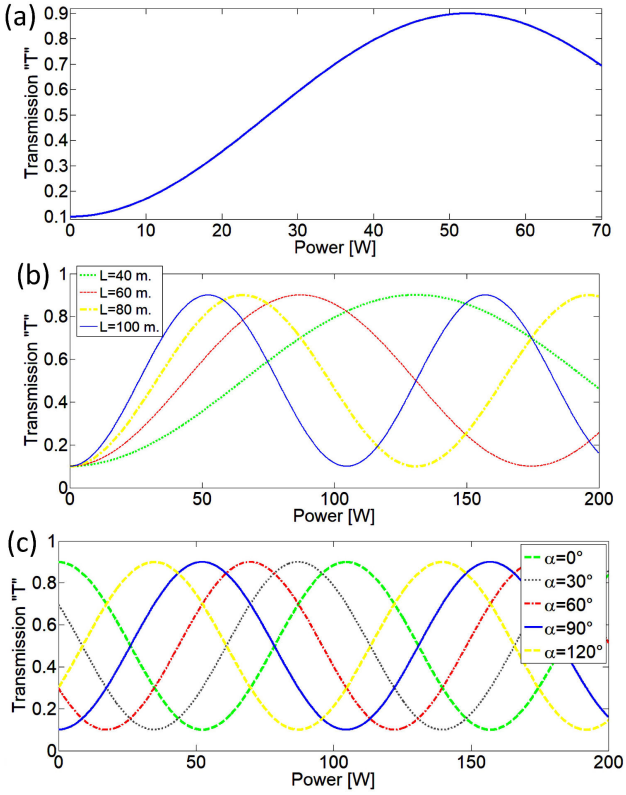

FIGURE 5. Transmission curve of the linear polarizer considering the NPR of an initial elliptical polarization state ($u = 2/\sqrt{5}$ and $v = 1/\sqrt{5}$), $A_c = 3/5$ and $\gamma_N = 1.5\ km^{-1}W^{-1}$: a) at fiber length $L = 100\ m$ and the linear polarizer oriented along of the vertical axis. b) at different fiber lengths and the linear polarizer oriented aligned with the vertical axis. c) at fiber length $L = 100\ m$ and different linear polarizer orientations with respect to the horizontal axis.

From this expression of the transmission through the linear polarizer aligned with the vertical axis (Eq. 15), it appears that for a longer length L of isotropic fiber a maximum transmission is achieved with a lower power P_π, as shown Fig. 5b. So, one observes that as length L decreases, the first maximum of transmission is reached at higher powers ($L = 80$ m yields $P_\pi = 65.44$ W, $L = 60$ m yields $P_\pi = 87.26$ W and $L = 40$ m yields $P_\pi = 130.89$ W).

On the other hand, when considering the same elliptical polarization state and the same parameters ($A_c = 3/5$, $\gamma_N = 1.5$ km^{-1}W^{-1}, $L = 100$ m); but assuming now that the orientation α of the polarizer is not fixed, then the expression of the transmission through the linear polarizer is function of this angle; Fig. 5c shows that a horizontal power displacement of the transmission curve takes place when the angle of the linear polarizer is changed.

4. 3D mapping of the pulse temporal profile

The 3D mapping technique, which is particularly useful to study pulse dynamics, consists of data processing from single-shot sequence measurements of the pulses over N consecutive periods, recorded with a fast oscilloscope, in order to build a 3D sequence of temporal profiles showing the pulses evolution over successive round-trips in the cavity. This temporal profile sequence in 3D is generated by the redistribution of the N consecutive periods (distributed over time) to N consecutive round-trips, as shown in Fig. 6. In this scheme, the consecutive periods are redistributed to consecutive round-trips with a reference system consisting in a short-time axis (covering the duration of the period), a long-time axis (showing the evolution over successive round-trips), and the intensity axis.

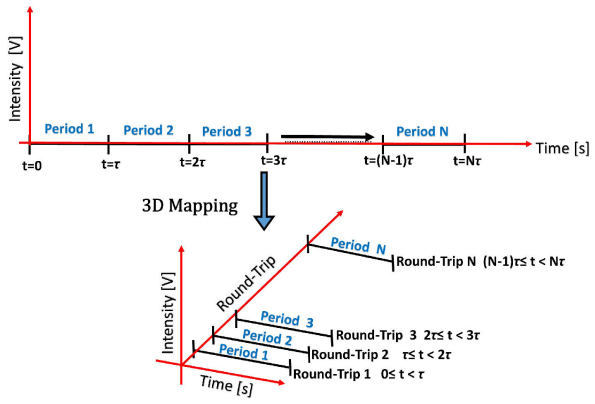

FIGURE 6. 3D mapping technique of the evolution over N round-trips of the pulses temporal profile.

The 3D mapping technique is illustrated by the following simulated example. This ideal case presents several pulses, each displaying a soliton envelope (sech^2 form); more precisely, there is a pulse conglomerate (five pulses with different peak intensities) that corresponds to shorter-wavelength spectral components and one single pulse that corresponds to longer-wavelength components; consequently, the single pulse and the pulse conglomerate propagate at different velocities. Fig. 7 shows different behaviors in the 3D mapping of this regime. When the ML-FL operates in the anomalous dispersion regime, the single pulse (longer-wavelength components) is delayed with respect to the pulse conglomerate (shorter-wavelength components); in this case the 3D mapping technique presents two behaviors when the single-shot measurement of oscilloscope is triggered on the pulse conglomerate (Fig. 7b) or on the single pulse (Fig. 7c). On the other hand, if the ML-FL operates with normal dispersion, the pulse conglomerate is delayed with respect to the single pulse, Figs. 7d and 7e show the 3D mapping in this case, when the single-shot measurement is triggered on the pulse conglomerate and on the single pulse, respectively.

All cases in Fig. 7 show that only one component (pulse conglomerate or single pulse) has a fixed temporal position over N round-trips, whereas the other one (single pulse or pulse conglomerate) has a constant temporal displacement to the right or left, known as temporal walk-off ($\triangle\tau/N$). The temporal walk-off (temporal displacement per round-trip) has a dependence with respect to the total dispersion D_T [ps/nm]

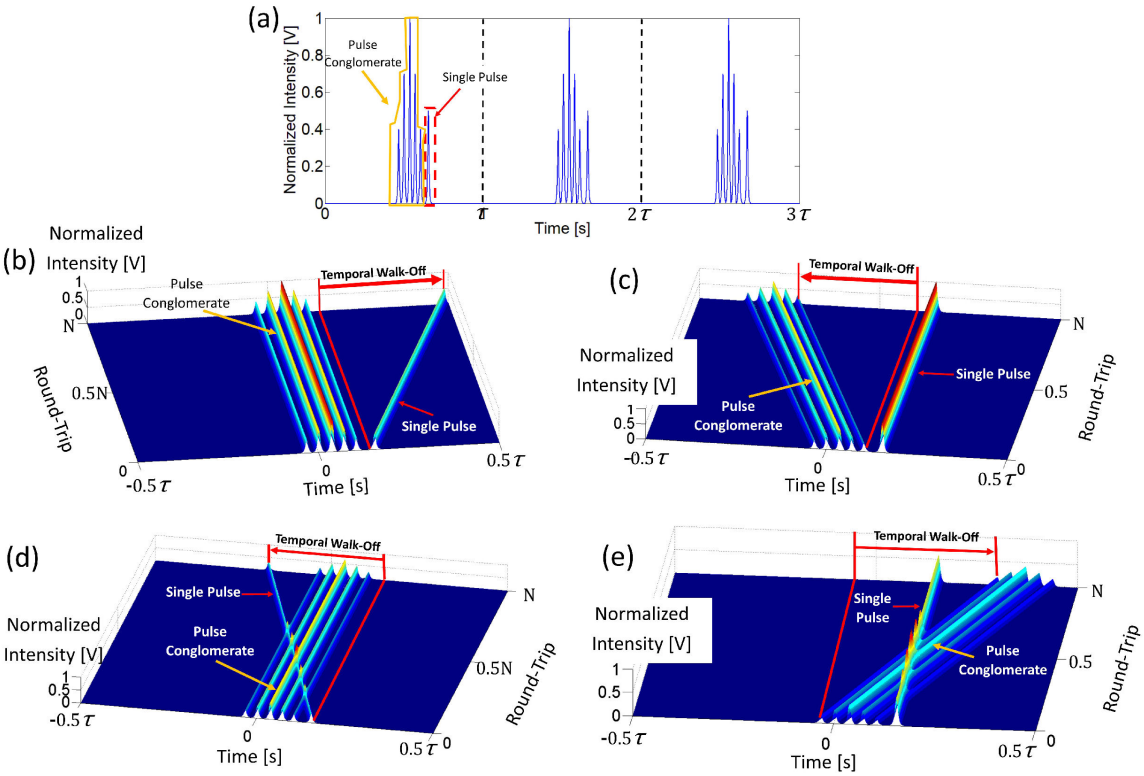

FIGURE 7. 3D mapping technique applied to characterize the temporal profile (a) of the pulse conglomerate coexisting with the single pulse analyze in anomalous dispersion when the fast oscilloscope trigger is on b) the pulse conglomerate or c) on the single pulse. The other case, in normal dispersion when the fast oscilloscope trigger is on d) the pulse conglomerate or e) the single pulse.

of the ML-FL and the spacing between two spectral components $\triangle\lambda$ [nm]:

$$\frac{\triangle\tau}{N} \approx D_T \triangle\lambda \tag{16}$$

4.1. Experimental 3D mapping of a noise-like pulse and bunches of solitons regime generated by a PML-FRL

A regime of noise-like pulse coexisting with bunches of solitons can be achieved in a PML-FRL. The experimental setup (Fig. 8) consists in 20 m of optical fiber in a ring configuration: 1 m of erbium-doped fiber (EDF, Liekki ER30-4/125) and 19 m of SMF-28. The EDF is the gain medium, which is pumped by a 980-nm laser diode (power of 300 mW) coupled through a wavelength division multiplexing (WDM) coupler. Following the EDF, an isolator is introduced, in Sec. 3 we analyzed the importance of this element which allows unidirectional signal propagation. Then, a polarization controller is inserted, which consists in a linear polarizer, a quarter wave retarder (QWR) and a variable wave retarder (VWR); the latter changes the polarization state by compression and rotation of a small portion of the fiber. The polarization controller ensures an elliptical polarization state, this polarization state and the linear polarizer are important to achieve the SA effect, as discussed in Sec. 3. A spool of 10 m of SMF-28 is placed at the polarization controller output, which introduces

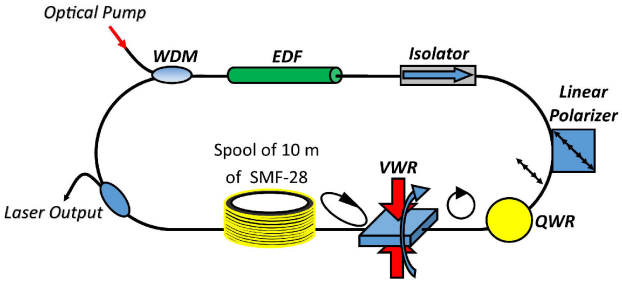

FIGURE 8. Experimental setup.

an anomalous dispersion in the ring cavity. It should be noted that a twist of 5 turns per meter is imposed to all fiber segments; the latter condition helps to eliminate the residual birefringence of the fiber and ensures that the ellipticity does not change during propagation.

The total dispersion in the cavity can be approximated from the values of the dispersion parameters, which are provided by the fiber manufacturer: the dispersion parameter of the SMF-28 is $D_{SMF28} = 0.017\ ps/nm/m$ and that of the EDF (Liekki ER30-4/125) is $D_{EDF} = -0.038$ ps/nm/m; so, the total dispersion in the cavity is

$$D_T = (19m)D_{SMF28} + (1m)D_{EDF} = 0.285\ \frac{\text{ps}}{\text{nm}} \tag{17}$$

this means that dispersion in the PML-FRL is anomalous.

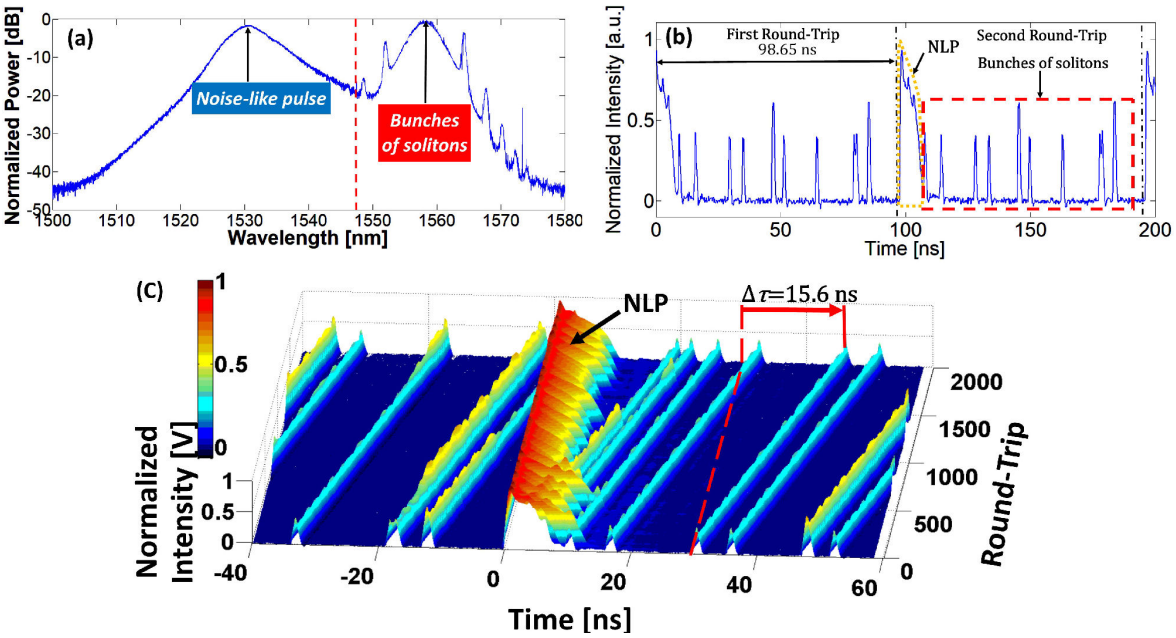

FIGURE 9. Regime of NLP and bunches of solitons. a) Optical spectrum. b) Temporal profile along two consecutive round-trips. c) 3D mapping of the temporal profile evolution along 2000 round-trips, the temporal walk-off is indicated (15.6 ns in 2000 round-trips)

There are only two degrees of freedom in the birefringence adjustments of the cavity: compression and rotation of the fiber in the VWR. For adequate adjustments of the VWR it is possible to produce a NLP coexisting with bunches of solitons. Fig. 9a shows the spectrum of this regime (measured at the fiber laser output with an optical spectrum analyzer (OSA), Anritsu MS9740A); the spectral component centered at 1531 nm corresponds to the NLP: the smooth trace is an indication of the NLP nature of this component. It is notable that the spectrum of a single NLP would present a spurious aspect, however because the OSA presents the average of a large amount of individual traces, the fluctuations are averaged out. On the other hand, the spectral component centered at 1558 nm corresponds to solitons; it is easily recognizable through the presence of side-bands known as Kelly side-bands [43]. The Kelly side-bands are originated from the dispersive waves generated by the soliton that comes into resonance with it [44]. The temporal profile of the pulses is measured at the fiber laser output using a 2 GHz photodetector and a fast oscilloscope (Tektronix DPO 7354C, bandwidth of 3.5 GHz), as shown in Fig. 9b. The complex envelope corresponds to the NLP and the low-intensity peaks correspond to the bunches of solitons. It is important to remark that the complete identification and characterization of this regime of NLP and bunches of solitons was presented in [29]. Besides, the pulse dynamics of this regime is analyzed in [36]. In contrast, the object of this work is only to illustrate an experimental 3D mapping measurement.

Since the pulses correspond to different spectral components, the NLP and the bunches of solitons have different velocities with respect to each other. Besides, the anomalous dispersion in the cavity ensures that the bunches of solitons (longer-wavelength component, 1558 nm) are delayed with respect to the NLP (shorter wavelength component, 1531 nm). Fig. 9c shows the 3D mapping of the pulses temporal profile for this regime, which is similar to the case illustrated in Fig. 7b; in this case the NLP presents a fixed position over 2000 round-trips and the bunches of solitons have a temporal walk-off (to the right) of 15.6 ns along 2000 round-trips (7.8 ps per round-trip), this experimental displacement is consistent with the theoretical temporal walk-off per round-trip of Eq. 16 (considering the total dispersion of the cavity $D_T = 0.285$ ps/nm and the spacing between the two spectral components $\triangle\lambda = 27$ nm) given by

$$\frac{\triangle\tau}{N} \approx 7.695 \text{ ps per round-trip} \tag{18}$$

5. Final comments

In this work, the basic elements in a PML-FRL were studied, in particular the SA mechanism achieved through NPR, and the use of linear polarizer was analyzed theoretically. It is important to note that in an experimental setup of PML-FRL, a uniform twist applied to the optical fiber introduces circular birefringence that rotates the polarization ellipse along propagation but does not alter its ellipticity, which ensures that NPR is uniform along the fiber, similarly to the theoretical study in Sec. 3 of the NPR effect in an isotropic fiber.

In general, the 3D mapping measurement provides deep information about the pulse dynamics, including their interactions and the behavior of the temporal envelope. This work focused in the study of the 3D mapping measurement of a pulse conglomerate coexisting with a single pulse that correspond to different wavelength components in anomalous or

normal dispersion regimes; the simulated behavior is contrasted with experimental results in which pulses associated with two different wavelength components coexist. The behavior in time domain tends to present one pulse or a group of pulses with fixed temporal position over successive round-trips, whereas the pulses associated with the other spectral component presents a temporal walk-off to the left or right. Besides, when only one spectral component exist, the 3D mapping measurement only shows pulses with fixed position over successive round-trips, as it can be observed for example in [34]; or in this case all pulses present a fixed temporal walk-off, as shown in [45].

Appendix

A. Non-linear polarization evolution in a twisted and circularly birefringent fiber.

This analysis is the essence and results of the reference [46]. The non-linear propagation in a twisted birefringent optical fiber, in the case of the continuous wave approximation (no variations with respect to time and small variations along propagation distance, $d^2C_\pm/dz^2 \approx 0$) can be expressed in terms of two coupled equations of the polarization components in the circular polarization base

$$\frac{dC_+}{dz} = i\rho C_+ + ike^{2iqz}C_- + i\gamma_N P(1-\frac{1}{3}A_c)C_+ \quad \text{(A.1)}$$

$$\frac{dC_-}{dz} = -i\rho C_- + ike^{-2iqz}C_+ + i\gamma_N P(1+\frac{1}{3}A_c)C_- \quad \text{(A.2)}$$

where, $C_\pm(z)e^{ik_0z} = (1/\sqrt{2})[E_x(z) \pm iE_y(z)]$; with:

- q is the rate of the twist applied to the fiber [rad/m]
- $\rho = (hq)/(2n)$ is the rotatory power, corresponding to a fraction $h/(2n)$ of the twist rate applied to the fiber (q) applied to the fiber ($h \approx 0.13, 0.16$ for silica fiber, so that $h/(2n) \sim 5\%$)
- $\gamma_N = (n_2\omega)/(cA_{\text{eff}})$ is the non-linear parameter and A_{eff} is the modal effective area
- $k = (\pi/L_B)$ is the parameter of linear birefringence and L_B is the beat length of the optical fiber
- $P = |C_+|^2 + |C_-|^2$ is the optical power
- $A_c = (|C_+|^2 - |C_-|^2)/P$ is the first Stokes parameter

The first two terms on the right side of Eqs. A.1 and A.2 are the contributions of circular and linear birefringence respectively. The factor of the complex exponential in the term of linear birefringence corresponds to the precession of the axes of birefringence, caused by the twist that is being applied to the fiber.

Due to the twist applied to the fiber, the linear birefringence averages out, so that the linear birefringence term in Eqs. A.1 and A.2 is neglected. Therefore, the two equations are decoupled, and the system has a trivial solution (with the first Stokes parameter $A_c \approx$ constant because changes of ellipticity are minimal). we proceed to solve the equations separately for each variable with integration limits $z = 0$ and $z = L$, L being the fiber length. The solution is summarized by the non-linear polarization evolution matrix, given by

$$NPE = \begin{pmatrix} e^{i(\rho L+\gamma_N P(1-\frac{1}{3}A_c)L)} & 0 \\ 0 & e^{i(-\rho L+\gamma_N P(1+\frac{1}{3}A_c)L)} \end{pmatrix} \quad \text{(A.3)}$$

The NPE matrix (Eq. A.3) contains the information of the two effects suffered by the optical field as it propagates through the fiber: a non-linear phase shift $\phi = \gamma_N PL$ and a linear and nonlinear rotation of the ellipse polarization state $r = \rho L - (1/3)\gamma_N PA_cL$. This consideration reduces the NPE matrix to

$$NPE = \begin{pmatrix} e^{i(\phi+r)} & 0 \\ 0 & e^{i(\phi-r)} \end{pmatrix} \quad \text{(A.4)}$$

Note: for the case of an ideal isotropic fiber, there will be no contribution of the linear rotation of the polarization ellipse ($\rho = 0$), so that $r = -(1/3)\gamma_N PA_cL$.

Acknowledgments

This work was funded by CONACyT Ciencia Básica project 253925.

1. S. Yamashita and K. Hotate, *Opt. Lett.* **26** (2001) 590. https://doi.org/10.1364/OL.26.000590
2. S. Wang, P. Lu, H. Liao, L. Zhang, D. Liu and J. Zhang, *J. Mod. Opt.* **60** (2013) 1892. https://doi.org/10.1080/09500340.2013.865801
3. Y. Zhang, W. Jin, H. B. Yu, M. Zhang, Y. B. Liao, H. L. Ho, M. S. Demokan, G. Stewart, B. Culshaw and Y. H. Li. *IEEE Photon. Technol. Lett.* **14** (2002) 1336. https://doi.org/10.1109/LPT.2002.801116
4. K. Ozgören, B. Öktem, S. Yilmaz, F. Ö. Ilday and K. Eken, *Opt. Express* **19** (2011) 17647. https://doi.org/10.1364/OE.19.017647

5. C. X. Yu, H. A. Haus, E. P. Ippen, W. S. Wong, and A. Sysoliatin, *Opt. Lett.* https://doi.org/10.1364/OL.25.00141825 (2000) 1418.
6. J. P. Lauterio-Cruz *et al*., *Laser Phys.* **27** (2017) 065107. https://doi.org/10.1088/1555-6611/aa6f6c
7. Irl N. Duling, *Opt. Lett.* **16** (1991) 539. https://doi.org/10.1364/OL.16.000539
8. M. E. Fermann, M. L. Stock, M. J. Andrejco and Y. Silberberg, *Opt. Lett.* **18** (1993) 894. https://doi.org/10.1364/OL.18.000894
9. V. J. Matsas, D. J. Richardson, T. P. Newson and D. N. Payne, *Opt. Lett.* **18** (1993) 358. https://doi.org/10.1364/OL.18.000358
10. A. Takada and H. Miyazawa. *IEEE Electron. Lett.* **26**(3) (1990) 216. https://doi.org/10.1049/el:19900145
11. D. J. Jones, H. A. Haus and E. P. Ippen, *Opt. Lett.* **21** (1996) 1818. https://doi.org/10.1364/OL.21.001818
12. N. J. Doran and David Wood, *Opt. Lett.* **13** (1988) 56. https://doi.org/10.1364/OL.13.000056
13. M. E. Fermann, F. Haberl, M. Hofer and H. Hochreiter, *Opt. Lett.* **15** (1990) 752. https://doi.org/10.1364/OL.15.000752
14. C. J. Chen, P. K. A. Wai and C. R. Menyuk, *Opt. Lett.* **20** (1995) 350. https://doi.org/10.1364/OL.20.000350
15. R. Paschotta and U. Keller, *Appl. Phys. B* **73** (2001) 653. https://doi.org/10.1007/s003400100726
16. M. Haiml, R. Grange and U. Keller, *Appl. Phys. B* **79** (2004) 331. https://doi.org/10.1007/s00340-004-1535-1
17. X. Tian, M. Tang, P. P. Shum, Y. Gong, C. Lin, S. Fu and T. Zhang, *Opt. Lett.* **34** (2009) 1432. https://doi.org/10.1364/OL.34.001432
18. R. Song, H. W. Chen, S. P. Chen, J. Hou and Q. S. Lu, *J. of Optics* **13**(3) (2011) 035201. https://doi.org/10.1088/2040-8978/13/3/035201
19. E. U. Rafailov, M. A. Cataluna and W. Sibbett, *Nature photonics* **1**(7) (2007) 395. https://doi.org/10.1038/nphoton.2007.120
20. R. Herda, O. G. Okhotnikov, E. U. Rafailov, W. Sibbett, P. Crittenden and A. Starodumov, *IEEE phot. technol. lett.* **18**(1) (2006) 157. https://doi.org/10.1109/LPT.2005.860376
21. S. Yamashita *et al.*, *Opt. Lett.* **29** (2004) 1581. https://doi.org/10.1364/OL.29.001581
22. A. Martinez and S. Yamashita, *Opt. Express* **19** (2011) 6155. https://doi.org/10.1364/OE.19.006155
23. M. N. Cizmeciyan, J. W. Kim, S. Bae, B. H. Hong, F. Rotermund and A. Sennaroglu, *Opt. Lett.* **38** (2013) 341. https://doi.org/10.1364/OL.38.000341
24. Z. Sun *et al.*, *ACS nano* **4** (2010) 803. https://doi.org/10.1021/nn901703e
25. O. Pottiez, R. Grajales-Coutiño, B. Ibarra Escamilla, E. A. Kuzin and J. C. Hernández-García, *Appl. Opt.* **50** (2011) E24. https://doi.org/10.1364/AO.50.000E24
26. H. Santiago Hernandez *et al.*, *Laser Phys.* **24** (2014) 015103. https://doi.org/10.1088/1054-660X/25/4/045106
27. X. Liu, L. Zhan, S. Luo, Z. Gu, J. Liu, Y. Wang and Q. Shen, *Opt. Express* **20** (2012) 7088. https://doi.org/10.1364/OE.20.007088
28. A. F. Runge, C. Aguergaray, R. Provo, M. Erkintal1 and N. G. Broderick, *Optical Fiber Technol.* **20** (2014) 657. https://doi.org/10.1016/j.yofte.2014.07.010
29. Y. E. Bracamontes-Rodríguez *et al*., *J. Opt.* **19**(3) (2017) 035502. https://doi.org/10.1088/2040-8986/aa5a41
30. F. Amrani, A. Haboucha, M. Salhi, H. Leblond, A. Komarov and F. Sanchez, *Appl. Phys. B* **99** (2010) 107. https://doi.org/10.1007/s00340-009-3774-7
31. P. Grelu and N. Akhmediev, *Nature Photonics* **6**(2) (2012) 84. https://doi.org/10.1038/nphoton.2011.345
32. W. Chang, J. M. Soto-Crespo, P. Vouzas and N. Akhmediev, *J. Opt. Soc. Am. B* **32** (2015) 1377. https://doi.org/10.1364/JOSAB.32.001377
33. E. Garcia Sanchez *et al.*, *Opt. Express* **24** (2016) 18917. https://doi.org/10.1364/OE.24.018917
34. E. Garcia-Sanchez, O. Pottiez, Y. Bracamontes Rodriguez, J. P. Lauterio-Cruz, H. E. IbarraVillalon, J. C. Hernandez-Garcia, M. Bello-Jimenez and E. A. Kuzin, *Laser Phys. Lett.* **13** (2016) 105106. https://doi.org/10.1088/1612-2011/13/10/105106
35. M. Liu, A-P Luo, W-C Xu and Z-C Luo. *Opt. Lett.* **41** (2016) 3912. https://doi.org/10.1364/OL.41.001181
36. O. Pottiez *et al*., *Laser Phys. Lett.* **14** (2017) 105101. https://doi.org/10.1088/1612-202X/aa8298
37. O. Svelto. *Principles of Laser.* 5th ed. (Springer US, New York, USA. 2010). pp. 339-341.
38. A. M. Saleh, R. M. Jopson, J. D. Evankow and J. Aspell, *IEEE Phot. Technol. Lett.* **2**(10) (1990) 714. https://doi.org/10.1109/68.60769
39. G. Agrawal. *Nonlinear fiber optics.* 5th ed. (Academic Press, New York USA 2013) pp. 6-11.
40. P. E. Powers. *Fundamentals of Nonlinear Optics.* 2nd ed. (CRC Press, Florida USA 2017) pp. 252-254.
41. K. Thyagarajan and A. Ghatak, *Lasers. Fundamentals and applications*, 2nd ed. (Springer Science+Business Media, LLC. 2010), pp. 315-317.
42. B. Daino, G. Gregori, and S. Wabnitz, *Opt. Lett.* **11** (1986) 42. https://doi.org/10.1364/OL.11.000042
43. S. M. J. Kelly, *IEEE Electron. Lett.* **28**(8) (1992) 806. https://doi.org/10.1049/el:19920508

44. N. J. Smith, J. K. Blow and I Andonovic, *IEEE J. Lightwave Technol.* **10** (1992) 1329. https://doi.org/10.1109/50.166771

45. S. V. Smirnov, S. Sugavanam, O. A. Gorbunov and D. V. Churkin, *Opt. Express* **25** (2017) 23122. https://doi.org/10.1364/OE.25.023122

46. S. F. Feldman, D. A. Weinberger and H. G. Winful, *J. Opt. Soc. Am. B* **10** (1993) 1191. https://doi.org/10.1364/JOSAB.10.001191